

A three-dimensional hybrid finite element – spectral boundary integral method for modeling earthquakes in complex unbounded domains

Gabriele Albertini^{1,2} | Ahmed Elbanna³ | David S. Kammer¹

¹Institute for Building Materials, ETH Zurich, Switzerland

²School of Civil and Environmental Engineering, Cornell University, Ithaca, NY, USA

³Department of Civil and Environmental Engineering, University of Illinois, Urbana-Champaign, IL, USA

Correspondence

David S. Kammer Email: dkammer@ethz.ch

Summary

We present a 3D hybrid method which combines the Finite Element Method (FEM) and the Spectral Boundary Integral method (SBIM) to model nonlinear problems in unbounded domains. The flexibility of FEM is used to model the complex, heterogeneous, and nonlinear part – such as the dynamic rupture along a fault with near fault plasticity – and the high accuracy and computational efficiency of SBIM is used to simulate the exterior half spaces perfectly truncating all incident waves. The exact truncation allows us to greatly reduce the domain of spatial discretization compared to a traditional FEM approach, leading to considerable savings in computational cost and memory requirements. The coupling of FEM and SBIM is achieved by the exchange of traction and displacement boundary conditions at the computationally defined boundary. The method is suited to implementation on massively parallel computers. We validate the developed method by means of a benchmark problem. Three more complex examples with a low velocity fault zone, low velocity off-fault inclusion, and interaction of multiple faults, respectively, demonstrate the capability of the hybrid scheme in solving problems of very large sizes. Finally, we discuss potential applications of the hybrid method for problems in geophysics and engineering.

KEYWORDS:

Finite Element Method, Spectral Boundary Integral Method, Hybrid Method, Dynamic Fracture, Earthquake Modeling

1 | INTRODUCTION

Earthquakes are a prime example of complex natural processes with far-from-equilibrium nonlinear dynamics at multiple scales. The lack of quantitative data on timescales capturing multiple large earthquake cycles is a fundamental impediment for progress in the field. Physics-based simulations provide the only path for overcoming the lack of data and elucidating the multi-scale dynamics and spatio-temporal patterns that extend the knowledge beyond sporadic case studies and regional statistical laws.

The multiscale nature of the earthquake phenomena is manifested as follows. Spatially, a moderate-size earthquake typically propagates over tens of kilometres. However, the physical processes governing the rupture propagation operates within a narrow region at the rupture tip, called the process zone, which may not exceed a few millimetres in size if realistic laboratory-based friction parameters are used.¹ Temporally, an earthquake event, where rapid slip occurs, only lasts for few to tens of seconds.

16 However, the time span between successive large earthquakes may be tens to hundreds of years.² Thus, there exists approximately
17 a decade of spatial and temporal scales that must be resolved in a target physics-based simulation of earthquakes and aseismic
18 slip. This necessitates innovation in modeling both the fast dynamic rupture with extreme localization and the slow quasi-static
19 slip, during the interseismic period, that exhibits gradual variations. This is a fundamental challenge in earthquake source physics
20 which has been a focus of computational earthquake mechanics over the past four decades.

21 Historically, numerical methods for simulating earthquakes and aseismic slip may be classified broadly into two categories:
22 boundary-based methods and domain-based methods. The boundary integral formulation enables reducing the spatial dimension
23 of the problem by one, by invoking the representation theorem of linear elastodynamics, transforming 2D problems into 1D
24 and 3D problems into 2D.^{3,4} The spectral formulation of the boundary integral equations has been transformative in seismic
25 applications (e.g. Lapusta et al.² and references therein). For example, Lapusta et al.² derived accurate adaptive time-stepping
26 algorithms and truncation of convolution integrals that enabled, for the first time, the consistent elastodynamic simulation of a
27 long sequence of events combining rapid slip during earthquake ruptures and slow deformation during the interseismic periods.
28 Nonetheless, the method is limited to homogeneous linear elastic bulk. While the method may be applied, in principle, to
29 heterogeneous linear elastic materials, the lack of a closed form representation of the Green's function either inhibits the method
30 from providing a well-defined solution to many problems of interest or makes it less computationally attractive. Furthermore,
31 the superior performance of the spectral approach and its computational efficiency is only possible for planar interfaces. This
32 precludes the representation of non-planar faults or direct incorporation of fault zone complexity (e.g. damage, and shear bands).

33 On the other hand, numerical methods based on bulk discretization such as the finite difference (FD) and finite element
34 methods have been used in simulating earthquake ruptures since mid-1970s and early 1980s with the pioneering works of
35 Boore et al.,⁵ Andrews,⁶ Das & Aki,⁷ Archuleta & Day,⁸ Day,⁹ Virieux & Madariaga,¹⁰ and others. These methods are more
36 flexible than the boundary integral approaches in handling heterogeneities, nonlinearities, and fault geometry complexities (see
37 Fig. 1a&b). In recent years, highly accurate formulations were introduced, including the spectral finite element,^{11,12,13,14,15}
38 the discontinuous Galerkin method,^{16,17,18,19,20} and higher-order FD schemes.^{21,22,23} A main computational challenge of these
39 methods is the need to discretize the whole bulk, which increases the computational demand by at least one order of magnitude
40 compared to the boundary integral formulation. Furthermore, the computational domain must be truncated at a sufficient distance
41 from the fault surface such that it would not affect the physical solution. While domain truncation has been achieved by the
42 introduction of several widely-used absorbing boundary conditions such as boundary viscous damping,²⁴ perfectly matching
43 layers,²⁵ and infinite elements,²⁶ these methods have limitations. Specifically, in all these methods, artificial reflections exist
44 to varying degrees and the absorbing surfaces must be taken sufficiently far from the fault surface to ensure solution accuracy.
45 Moreover, attempts to perform cycle simulations using these volume-based methods are rare and have been restricted mainly to
46 the quasi-dynamic limit.²⁷ This is partially due to the high spatial discretization cost and the lack of a systematic approach to
47 handle both dynamic and quasi-dynamic calculations in the same framework which is required for simulating both earthquake
48 ruptures and interseismic slow deformations. Another challenge in these methods is defining fault loading. Currently, this is
49 done by applying displacement-controlled loading at the far boundaries of the simulation box. This, however, makes the fault
50 stressing rate dependent on where the domain is truncated. This problem is solved approximately in the SBI formulation by
51 loading the fault directly through back-slip.

52 Both bulk and boundary approaches have their merits and limitations. The limitations are evident in 3D simulations where
53 computational complexity grows like the element size to the fourth power rendering high resolution models a computational
54 bottleneck. To that end, this paper proposes a new hybrid numerical scheme, for the full three dimensional elastodynamic
55 problem, that combines the 3D FE method and the 2D SBI equation method to efficiently model fault zone nonlinearities and
56 heterogeneities with high resolution while capturing large-scale elastodynamic interactions in the bulk. The main idea of the
57 method is to enclose the heterogeneities in a virtual strip that is introduced for computational purposes only (see Fig. 1c). This
58 strip is discretized using a volume-based numerical method, chosen here to be the finite element method due to its popularity and
59 flexibility in handling complex geometry and arbitrary bulk heterogeneities. The top and the bottom boundaries of the virtual
60 strip are handled using the independent SBI formulation⁴ with matching discretization. The coupling between the two methods
61 is achieved through enforcing continuity of displacement and traction at the virtual boundaries. The current work extends recent
62 work by the authors and their groups over the past few years which first developed the hybrid scheme for the 2D dynamic anti-
63 plane problem combining finite difference and spectral boundary integral methods,²⁸ and the 2D dynamic in-plane problem
64 using the finite element method for bulk discretization in the hybrid scheme.²⁹ Prior work has demonstrated the accuracy and
65 computational efficiency of the coupled approach and its potential for modeling dynamic ruptures with high resolution fault

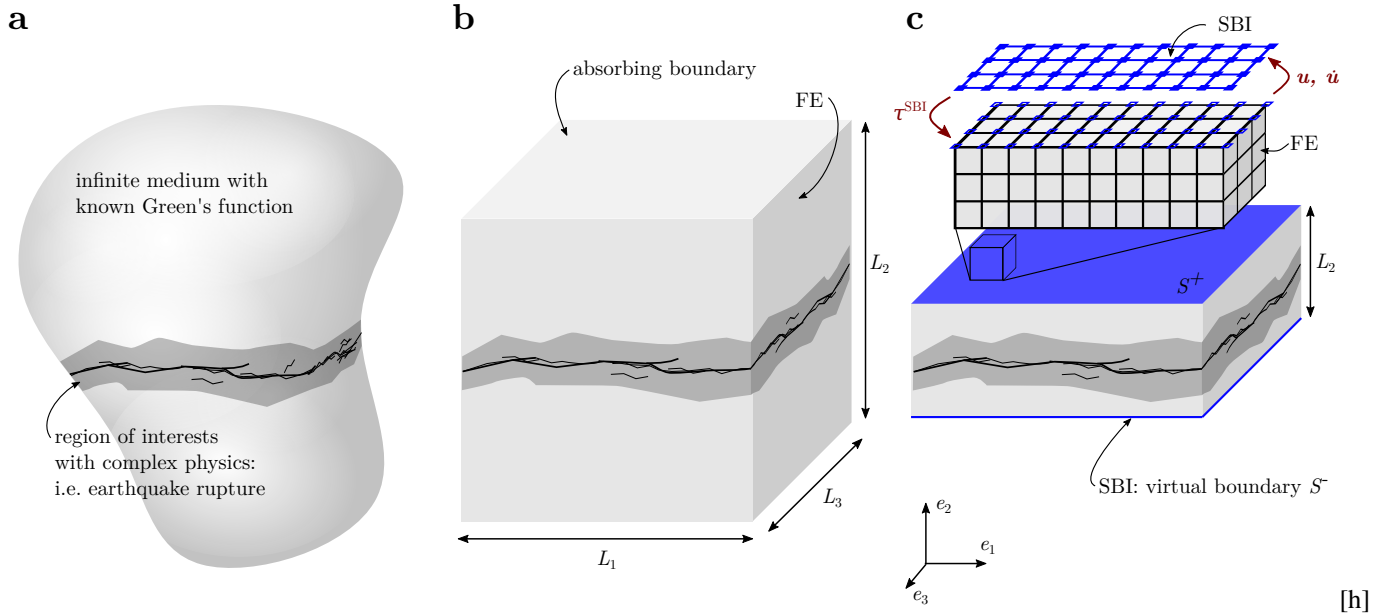


FIGURE 1 Schematic representation of the physical problem (a), its representation using a domain-based method such as FE (b), and using the hybrid method (c). The hybrid method couples a domain-based method with a boundary-based method, through the communication of nodal traction τ^{SBI} , displacement \mathbf{u} , and velocity $\dot{\mathbf{u}}$ at the boundaries of the virtual strip, S^\pm .

66 zone physics³⁰ as well as extension to the quasi-dynamic limit and cycle simulations.³¹ The current extension to the full three
 67 dimensional case represents the culmination of these efforts.

68 The remainder of this paper is organized as follows. In Section 2, we describe the physical model (Section 2.1), and the
 69 numerical methods to solve it, which includes the finite-element method (Section 2.2), the spectral boundary integral method
 70 (Section 2.3), and their coupling – the hybrid method (Section 2.4). In Section 3, we validate the hybrid method using the
 71 benchmark problem TPV3³² of the Southern California Earthquake Center. Next, we demonstrate the capabilities of the new
 72 hybrid method on more complex problems. We consider a low velocity fault zone in Section 4, a low velocity inclusion at a
 73 distance from the fault in Section 5, and interacting faults in Section 6. Finally, we discuss the advantages of the hybrid method
 74 in terms of computational cost in Section 7 and draw conclusions in Section 8.

75 2 | METHOD

76 2.1 | Physical Model

77 We solve the fully dynamic three-dimensional problem of a rupture propagating along a fault embedded in an elastic solid. The
 78 conservation of linear momentum within the elastic domain Ω is given by

$$\rho \ddot{u}_i - \frac{\partial \sigma_{ij}}{\partial x_j} = 0 \quad \text{in } \Omega \quad (1)$$

79 where ρ is the material density, u_i the displacement vector, with the “dot” being the derivative with respect to time t , σ_{ij} the
 80 Cauchy stress tensor, and x_j the coordinate vector. Body forces are neglected. Dirichlet boundary conditions are applied on S_u
 81 and Neumann boundary conditions are applied on S_τ

$$u_i = \bar{u}_i \quad \text{on } S_u \quad (2)$$

$$\sigma_{ij} n_j = \bar{\tau}_i \quad \text{on } S_\tau, \quad (3)$$

82 where n_i is the normal vector to the surface S_τ . Initially, the domain is assumed to be in equilibrium, and, hence, the initial
 83 conditions are given by $u_i(0) = u_i^0$ and $\dot{u}_i(0) = 0$. We assume linear elastic material behavior:

$$\sigma_{ij} = \lambda \delta_{ij} \varepsilon_{kk} + 2\mu \varepsilon_{ij} \quad (4)$$

84 with the infinitesimal strain tensor $\epsilon_{ij} = (\partial u_i / \partial x_j + \partial u_j / \partial x_i) / 2$ and the Lamé parameters λ, μ describing the elastic properties
85 of the material.

86 The fault transmits stresses from one half-space to the other through interface tractions. We focus on tangential (friction)
87 interaction and impose non-penetration/non-opening conditions to the normal component of the fault surfaces S_f^\pm . The local
88 slip vector, which corresponds to the tangential fault opening vector, is given by

$$\delta_i = R_{ij}(u_j^+ - u_j^-) \quad \text{on } S_f^\pm, \quad (5)$$

89 where R_{ij} is the global-to-local rotation matrix and + and - indicate the upper and lower fault sides, respectively. Local slip
90 δ is the amplitude of δ_i . The fault is governed by a stick-slip behavior that is described by two states. A sticking section of the
91 fault is described by:

$$\dot{\delta} = 0 \quad \text{and} \quad \tau \leq \tau^s \quad (6)$$

92 where $\dot{\delta}$ is slip rate, τ the amplitude of the fault shear traction vector and τ^s the fault strength. A sliding fault section is described
93 by:

$$\dot{\delta} > 0 \quad \text{and} \quad \tau = \tau^s. \quad (7)$$

94 A constitutive law is applied to model the fault strength evolution. For simplicity, we apply a linear slip-weakening friction
95 law,³³ which is given by:

$$\mu(\delta) = \begin{cases} \mu_s - (\mu_s - \mu_k) \delta / \delta_c & \text{for } \delta < \delta_c \\ \mu_k & \text{for } \delta \geq \delta_c \end{cases} \quad (8)$$

96 where μ_s and μ_k are the static and kinetic friction coefficient, respectively, and δ_c is the characteristic slip length to reach residual
97 strength. The fault strength is then given by $\tau^s = \sigma^n \mu(\delta)$, where σ^n is the normal stress. Other friction laws, such as rate-and-state
98 friction,^{34,35} could also be applied in a similar framework, as shown by Kaneko et al.¹⁵

99 2.2 | Finite Element Method (FEM)

100 The finite element method is based on a variational formulation of the governing equation and applies a discretization based
101 on shape functions to find an approximate solution to the physical problem presented in Sec. 2.1. A detailed description can be
102 found in standard textbooks.³⁶ The FEM approach transforms the strong form, *i.e.*, the governing equation (1), to the weak form
103 by multiplying it with the test functions $\hat{u}(x)$, integrating it over the domain, and applying Green's identity, which results in:

$$\int_{\Omega} \rho \ddot{u}_i \hat{u}_i \, d\Omega + \int_{\Omega} \sigma_{ij} \frac{\partial \hat{u}_i}{\partial x_j} \, d\Omega - \int_{S_\tau} \bar{\tau}_i \hat{u}_i \, dS - \int_{S_f} \tau_i \hat{u}_i \, dS = 0. \quad (9)$$

104 Test functions are chosen smooth enough, such that all steps are well defined and vanish on the Dirichlet boundary. By choosing
105 suitable interpolation functions, $N_I(x_J) = \delta_{IJ}$, and test function $\hat{u}(x) = \sum_I N_I(x) u_I(t)$, where the subscript I represent the
106 node index, $u_I(t)$ becomes the nodal displacements. Using this standard FE approach, the weak form can be expressed as the
107 following matrix equation

$$\mathbf{M}\ddot{\mathbf{u}} + \mathbf{K}\mathbf{u} - \mathbf{f} - \mathbf{B}\boldsymbol{\tau} = \mathbf{0} \quad (10)$$

108 where $\ddot{\mathbf{u}}$ denotes the second time derivative of the displacement vector, \mathbf{M} and \mathbf{K} are the mass and stiffness matrix, respectively,
109 \mathbf{B} is a fault rotation-area matrix, $\boldsymbol{\tau}$ is the fault traction vector, and \mathbf{f} is the force vector from Neumann boundary conditions.

110 We apply an explicit central-difference time integration formulation with a predictor-corrector formulation. The step-by-step
111 procedure follows:

$$\dot{\mathbf{u}}_{t+1}^{pred} = \dot{\mathbf{u}}_t + \Delta t \ddot{\mathbf{u}}_t \quad (11)$$

$$\mathbf{u}_{t+1} = \mathbf{u}_t + \Delta t \dot{\mathbf{u}}_{t+1}^{pred} \quad (12)$$

$$\Delta \ddot{\mathbf{u}} = (-\mathbf{K}\mathbf{u}_{t+1} + \mathbf{f} + \mathbf{B}\boldsymbol{\tau}_{t+1}) \mathbf{M}^{-1} - \ddot{\mathbf{u}}_t \quad (13)$$

$$\dot{\mathbf{u}}_{t+1} = \dot{\mathbf{u}}_{t+1}^{pred} + \frac{1}{2} \Delta t \Delta \ddot{\mathbf{u}} \quad (14)$$

$$t = t + \Delta t \quad (15)$$

112 where the subscript indicates the time step and Δt is the current incremental time step, which is required to satisfy the Courant-
113 Friedrichs-Lewy condition.³⁷ We apply a lumped mass matrix, which simplifies the computation of the inverse mass matrix and
114 reduces computational cost of the time-integration scheme. The fault rotation matrix is scaled by the fault-surface area associated
115 with each fault-split-node and thus transforms the fault traction vector $\boldsymbol{\tau}$ to a nodal force vector.

116 The fault traction vector $\boldsymbol{\tau}_{t+1}$ in Eq. (13) is computed by a forward Lagrange multiplier method,³⁸ which uses a prediction
 117 procedure to pre-computes the slip rate for the next time step. A similar approach was applied in spectral-element simulations.¹⁵
 118 We denote a fault discontinuity as $[[A]] = (A_+ - A_-)$ where subscript + and - indicate the upper and lower fault sides,
 119 respectively. The predicted slip rate during the next time step if no fault tractions were applied is given by

$$[[\dot{\mathbf{u}}_{t+3/2}]] = [[\dot{\mathbf{u}}_{t+1}^{pred} - \frac{\Delta t}{2} \ddot{\mathbf{u}}_t - \Delta t \mathbf{M}^{-1} (\mathbf{K}\mathbf{u}_{t+1} - \mathbf{f})]]. \quad (16)$$

120 We use the slip-rate predictor $[[\dot{\mathbf{u}}_{t+3/2}]]$ because the no-slip-rate condition $[[\dot{\mathbf{u}}_{t+3/2}]] = 0$ will ensure that the interface remains
 121 stuck and hence $[[\mathbf{u}_{t+2}]] = [[\mathbf{u}_{t+1}]]$. Using Eq. 16, we can compute the traction required to maintain slip and impose stick
 122 condition on the fault by

$$\tilde{\boldsymbol{\tau}}_{t+1} = \frac{1}{2} \mathbf{Z} [[\dot{\mathbf{u}}_{t+3/2}]], \quad (17)$$

123 where \mathbf{Z} is the fault impedance matrix given by $\mathbf{Z}^{-1} = \Delta t (\mathbf{M}_+^{-1} \mathbf{B}_+ + \mathbf{M}_-^{-1} \mathbf{B}_-)/2$ and the following fault traction balance was
 124 applied $\boldsymbol{\tau} = -\boldsymbol{\tau}_+ = \boldsymbol{\tau}_-$. The actual fault traction is computed by applying the stick-slip conditions given by Eq. (6) and Eq. (7):

$$\boldsymbol{\tau}_{t+1} = \begin{cases} \tilde{\boldsymbol{\tau}}_{t+1} & \text{if } \tilde{\boldsymbol{\tau}}_{t+1} \leq \boldsymbol{\tau}_{t+1}^s \text{ (stick)} \\ \boldsymbol{\tau}_{t+1}^s & \text{otherwise (slip)} \end{cases} \quad (18)$$

125 where $\boldsymbol{\tau}_{t+1}$ and $\tilde{\boldsymbol{\tau}}_{t+1}$ are individual entries in $\boldsymbol{\tau}_{t+1}$ and $\tilde{\boldsymbol{\tau}}_{t+1}$, respectively, and $\boldsymbol{\tau}_{t+1}^s$ is the fault strength at each split-node (node
 126 indicator is omitted for simplicity) and is governed by Eq. (8).

127 2.3 | Spectral Boundary Integral Method (SBIM)

128 Boundary integral methods have the advantage of modeling the wave propagation problem in the entire domain Ω by using an
 129 integral relationship (in space and time) between the displacements and the tractions along the boundary of the domain $\partial\Omega$.
 130 The advantage lies in reduced computational cost and increased accuracy with respect to a finite-element or finite-difference
 131 method. For these reasons, boundary integral methods have been used extensively since the mid-1980s to study crack propagation
 132 problems.^{39,40,41,42,43,44,45,46,47,3,48}

133 Consider the displacements and tractions at a the boundary of an semi-infinite half space with the boundary lying on the e_1, e_3
 134 plane and the domain being infinite in the e_2 direction. Following the process described in Geubelle and Rice,⁴ the elastodynamic
 135 response of a 3D elastic half space is given by

$$\boldsymbol{\tau}_i^{\text{SBI}}(x_1, x_3, t) = \boldsymbol{\tau}_i^\infty(x_1, x_3, t) - \eta_{ij} \frac{\mu}{c_s} \dot{u}_j(x_1, x_3, t) + s_i(x_1, x_3, t), \quad (19)$$

136 where η_{ij} is a diagonal matrix with $\eta_{11} = \eta_{33} = 1$ and $\eta_{22} = c_s/c_p$. c_p and c_s are the longitudinal and shear wave speeds of
 137 the material, respectively. Eq. (19) states that the traction at the surface of the half space, $\boldsymbol{\tau}_i^{\text{SBI}}$, equals the far field traction, $\boldsymbol{\tau}_i^\infty$,
 138 plus a ‘‘radiation damping’’ term, $\eta_{ij} \frac{\mu}{c_s} \dot{u}_j^\pm$, and a spatiotemporal integral term s_i . In this formulation the elastodynamic response
 139 is separated between local and nonlocal contributions. s_i represents the nonlocal elastodynamic long-range interaction between
 140 different parts of the surface, and the local effect $\eta_{ij} \frac{\mu}{c_s} \dot{u}_j$ represents wave radiation from the surface.

141 We use the spectral approach⁴⁹ for computing s_i which involves a Fourier transform in space and a convolutions in time,
 142 where the displacement history is convolved with the elastodynamic kernels. Please refer to independent formulation in⁴⁹ for
 143 the derivation of the kernels and details for computing the nonlocal term, s_i .

144 2.4 | Hybrid FEM-SBIM Method

145 The hybrid method consists in coupling the FEM and the SBIM at the boundaries S^\pm , where the FE-domain is truncated (see
 146 Fig. 1c). At S^\pm , which we refer to as the virtual boundary, we apply an exact elastodynamic transparent boundary condition
 147 using the SBIM, which accounts for wave propagation in the infinite half-space beyond the FE truncation. Depending on the
 148 FE scheme, Neumann or Dirichlet boundary conditions might be more suitable. For example, Dirichlet boundary conditions
 149 might result in a more stable algorithm. Here, we present the Neumann approach (for the Dirichlet approach please refer to Ma
 150 et al.²⁹). We impose continuity condition at the boundaries S^\pm , which results in the FE force \mathbf{f} being equal to the SBI traction
 151 $\boldsymbol{\tau}^{\text{SBI}}$ multiplied by a rotation-area matrix \mathbf{B}^{SBI} .

152 The Neumann approach consists in solving the boundary integral relation, Eq. (19), by using the displacements and velocity
 153 computed from the FEM. The resulting traction is then applied as a Neumann boundary condition in the FEM. A time step of
 154 the hybrid method is computed as follows:

- 155 1. FE compute explicit time integration Eq. (12) and predict velocity Eq. (11)
- 156 2. copy \mathbf{u}_{t+1} and $\dot{\mathbf{u}}_{t+1}^{pred}$ from FE to SBI
- 157 3. SBI compute response of half space, τ^{SBI} , for given displacement history $u(x_1, x_3, t)$ and current velocity prediction $\dot{\mathbf{u}}_{t+1}^{pred}$
- 158 Eq. (19)
- 159 4. apply SBI interface traction as Neumann boundary condition in FE: $\mathbf{f} = \mathbf{B}^{SBI}\boldsymbol{\tau}^{SBI}$
- 160 5. FE compute friction traction $\boldsymbol{\tau}_{t+1}$ using Eq. (18)
- 161 6. FE compute acceleration increment Eq. (13)
- 162 7. FE correct velocity Eq. (14)

163 Alternative coupling methods, *e.g.*, Lagrange multiplier, could also be applied. However, as we will show in Sec. 3, the simple
 164 staggered approach proposed here provides excellent accuracy and is optimal in terms of computational efficiency. Further, in
 165 the finite-element domain, we apply 8-node linear hexagonal elements in a regular mesh in all presented problems.

166 3 | BENCHMARK PROBLEM TPV3: EARTHQUAKE RUPTURE IN UNBOUNDED 167 HOMOGENEOUS DOMAIN

168 3.1 | Setup

169 We verify the hybrid method with the benchmark problem TPV3 from the SCEC Dynamic Rupture Validation exercises
 170 (<https://strike.scec.org/cvws/>). The problem considers a planar fault, governed by linear slip-weakening friction, embedded
 171 in a homogeneous linear elastic bulk (see Fig. 2a). The elastic bulk has a density of $\rho = 2670 \text{ kg/m}^3$, pressure wave speed
 172 $c_p = 6000 \text{ m/s}$, and shear wave speed $c_s = 3464 \text{ m/s}$. The friction properties are uniform and characterized by $\mu_s = 0.677$,
 173 $\mu_k = 0.525$ and $d_c = 0.4 \text{ m}$. A uniform background shear, $\tau_0 = 70 \text{ MPa}$, and normal stress, $\sigma_0 = 120 \text{ MPa}$, are applied. The
 174 rupture is nucleated at the center of the fault over a square patch of size a^2 by instantaneously increasing the shear stress to a
 175 value higher than the static friction. After nucleation, the rupture quickly propagates across the entire fault.

176 Note that this problem does not present any off-fault non-linearities and the fault is planar. Hence, the hybrid method is
 177 not required for this particular problem, which could be solved solely by the SBIM. However, we use this problem to verify
 178 the hybrid method by comparing the results with the reference solution of the SBIM. Additional examples, which do include
 179 non-linearities that require the hybrid method, will be presented in the following sections.

180 Additionally, in this example (as well as in Sec. 4 and 5) the fault (*i.e.*, the 13 plane) represented a symmetry plane. The
 181 implication of this are twofold: (i) the normal stress on the fault remains constant throughout the simulation and so do the
 182 peak and residual friction strengths (ii) there is no need of explicitly modelling the bottom half space of the simulation domain
 183 (*i.e.*, $x_2 < 0$), which is taken into account for when applying the frictional traction on the fault by enforcing $[[u_2]] = 0$ and
 184 $\sigma_{22} = \text{const}$. Note that, by applying the hybrid method, we model the entire top (*i.e.*, $x_2 > 0$) half space. However, there are
 185 two additional symmetry planes: the 12 plane and the 23 plane. Thus, the FE computational domain could be further reduced
 186 by using the appropriate boundary conditions.

187 3.2 | Results

188 We present the results of the hybrid method with a virtual strip width $L_2 = 4\Delta x$ (see Fig. 2b) and compare it with the reference
 189 solution. For both methods we use the same spatial discretization with $\Delta x = 50 \text{ m}$. Rupture front position (see Fig. 3a), and stress
 190 and slip time history at three stations (see Fig.3b) show excellent agreement between the hybrid method and the SBIM. Fig. 4
 191 shows the shear stress σ_{12} field on one quadrant of the virtual strip. The rupture front is characterized by an abrupt change from
 192 peak to residual strength. The excellent agreement with the reference solution (Fig. 3) demonstrates that the the elastodynamic
 193 boundary condition enforced on the planes S^\pm does not cause any artificial wave reflection even though the virtual strip is
 194 extremely thin.

195 We perform a mesh convergence study of the hybrid method and show that the L_2 norm of the error, computed using a
 196 reference solution with $\Delta x = 25 \text{ m}$, decreases linearly (see Fig. 5a). The hybrid method combines linear finite elements with a

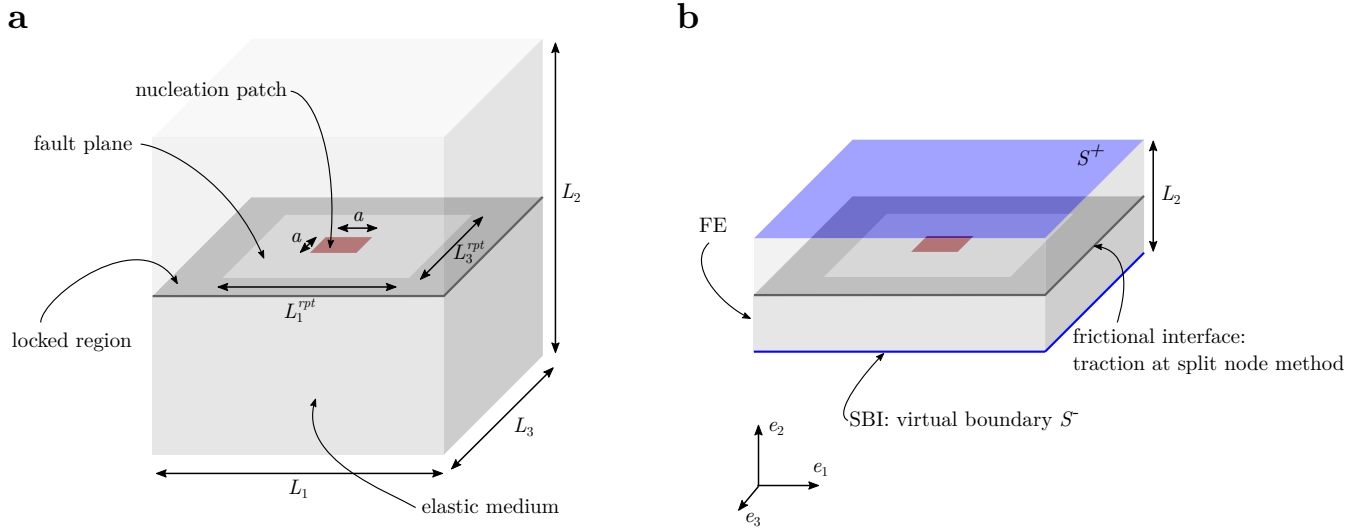


FIGURE 2 Setup of benchmark problem TPV3. (a) Earthquake rupture in unbounded domain with nucleation over square region of size $a = 3$ km and fault regions of size $L_1^{rpt} = 30$ km and $L_3^{rpt} = 15$ km. (b) Hybrid setup: FE domain with SBI as elastodynamic boundary condition.

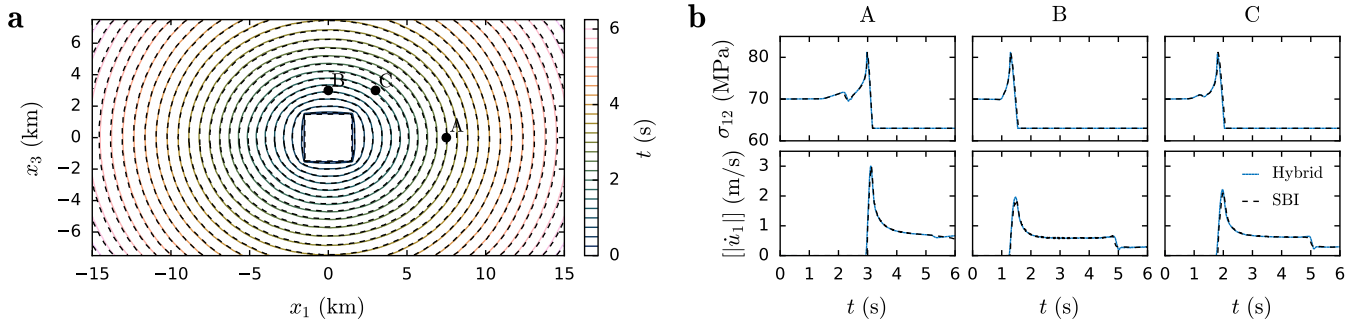


FIGURE 3 Benchmark problem TPV3 solved using hybrid method (blue lines) and using the SBIM (dashed black lines). (a) Contour of rupture front position each 0.5s. (b) Fault shear stress, σ_{12} , and slip rate, \dot{u}_1 , at three stations A, B, and C with position shown in (a).

197 higher precision spectral boundary method. Therefore, the convergence rate of the hybrid method corresponds to the rate of the
 198 least accurate of the methods it combines, *i.e.*, the linear finite element method. Hence, the hybrid method does not loose any
 199 accuracy compared to a fully FEM model.

200 Since we are dealing with a dynamic problem, we also show the temporal evolution of the error at station C (see Fig. 5b). The
 201 error is initially zero because the waves and the rupture have not reached the station yet. At $t \approx 1.8$ s, the rupture reaches the
 202 station (see also Fig. 3b) and hence the error increases rapidly. It then remains approximately constant while the fault continues
 203 to slide until reflected waves from the boundary between rupture region and locked region (not the virtual boundary) reach the
 204 station. At this point, we notice a temporary drop in the error before it increases again to the same level of error observed before.
 205 Overall, we find that the error remains mostly constant over the duration of the simulation and decreases with mesh refinement.

206 Even though this benchmark problem is linear elastic and does not necessitate the use of the hybrid method, it illustrates
 207 its capability of efficiently and accurately truncating elastic waves in the vicinity of the fault with no artificial reflections from
 208 the virtual boundaries, S^\pm , which were only two elements away from the fault. In more complex scenarios, this virtual strip
 209 might need to be larger in order to fully describe the source of non-linearities or heterogeneity. Nevertheless, this efficient near-
 210 field truncation algorithm enables us to decrease the domain of finite-element discretization, compared to a fully FEM model,

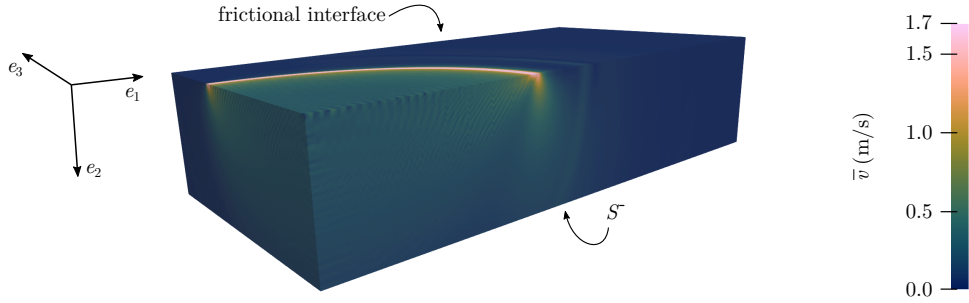


FIGURE 4 Benchmark problem TPV3 solved using hybrid method. Velocity magnitude field, \bar{v} , at $t = 3.4$ s. For better visualization we applied a much thicker virtual strip, *i.e.*, $L_2 = 10$ km instead of $L_2 = 0.2$ km as applied for simulations shown in Fig. 3.

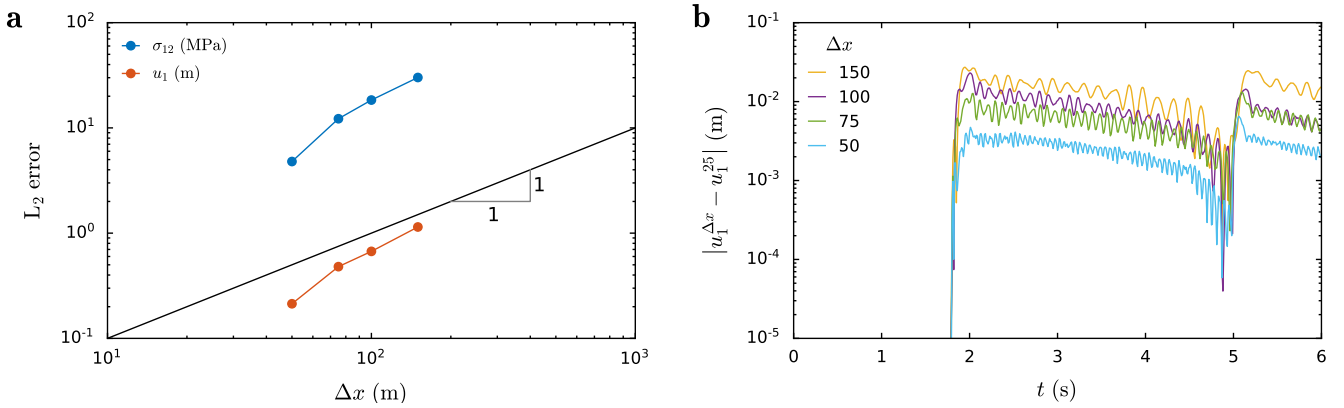


FIGURE 5 Benchmark problem TPV3 solved with hybrid method – mesh convergence study (a) L_2 error as function of mesh size Δx computed over the entire fault at $t = 3$ s. (b) Absolute error as function of time at station C.

211 and apply a volumetric mesh only in a narrow strip around the fault, which results in considerable savings in terms of both
 212 computational time and memory, as we will discuss further in Sec. 7.

213 4 | EARTHQUAKE RUPTURE WITH LVFZ: PULSE-LIKE BEHAVIOUR

214 4.1 | Setup

215 The previous example was a benchmark problem and could have been solved by a boundary-element approach without any
 216 discretization of the bulk. Hence, the hybrid method was not required. In the following, we will consider more complex problems,
 217 which require volumetric discretization. First, we consider a slip-weakening fault with a low velocity fault zone (LVFZ). LVFZ
 218 are found in most mature faults, where the near fault rock is considerably damaged and, as a consequence, has a reduced wave
 219 speed ranging from 20% to 60% with respect to the host rock.^{50,51,52,53,54} In 2D setups, when the reduction is high enough, the
 220 rupture behaves like a pulse. The results presented here will confirm this behavior on a 3D setup.

221 We consider a velocity reduction of 20% with respect to the surrounding host rock, which has the same elastic properties as
 222 in Sec. 3. The fault geometry is given in Fig. 6, and is governed by linear slip-weakening friction with $\mu_s = 0.677$, $\mu_k = 0.564$,
 223 and $d_c = 0.2$. The fault is subjected by a uniform background shear $\tau^0 = 27.5$ MPa and normal $\sigma^0 = 44$ MPa stress. We nucleate
 224 the fault rupture over a square region of size a^2 by instantaneously applying a loading traction of 31 MPa, which locally exceeds
 225 the peak friction strength.

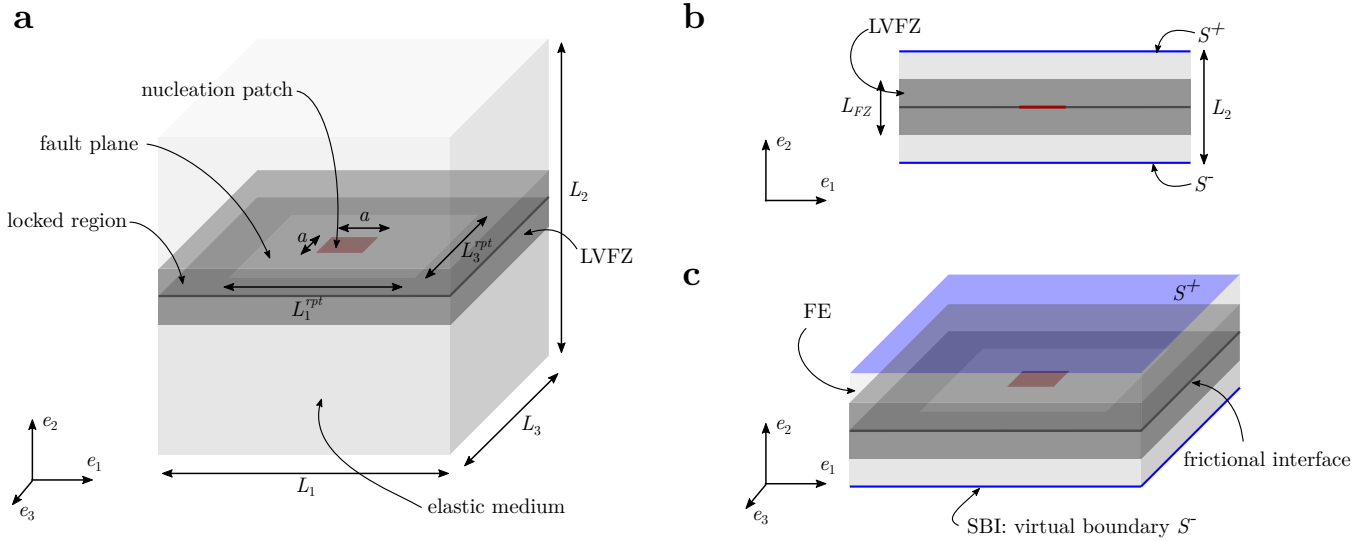


FIGURE 6 Setup of example earthquake rupture in unbounded domain with LVFZ. (a) Fault plane geometry and nucleation patch are analogous to the previous example but with a larger size: $L_1^{rpt} = 60$ km, $L_3^{rpt} = 30$ km, and $a = 3.2$ km. The fault zone region surrounding the fault is more compliant and presents a thickness of $L_{FZ} = 1.6$ km. (b) Hybrid setup: FE virtual strip with $L_2 = 2$ km and with SBI as elastodynamic boundary condition.

4.2 | Results

As a result of the nucleation procedure, the rupture front quickly propagates radially and eventually spans the entire fault (see Fig. 7). When a dynamic rupture propagates, it radiates elastic waves, which are then reflected at the boundary of the LVFZ.⁵⁴ Depending on the incident angle, the reflected wave can have an inverted polarization and cause unloading of the fault and generate a slip pulse. This effect is also observed in our 3D simulations and is shown in Fig. 7b, station C, and in Fig. 8. The reflected wave causes the rupture to split into a pulse-like rupture, followed by a crack-like rupture.

The rapid acceleration and deceleration of a slip pulse are a source of high frequencies (see Fig. 9b Station C) and cause oscillations in slip velocity, trailing the rupture front (see Fig. 8). These oscillations do not affect the rupture propagation and disappear with further mesh refinement and regularized friction laws.⁵⁵ Additionally, numerical damping, which is not used here, is often applied to minimize such high frequencies. Since this problem cannot be solved with the SBI method, we validate the results of the hybrid method by varying the width of the virtual strip, L_2 , and confirm that the solution is independent on the location of the elastodynamic boundary condition.

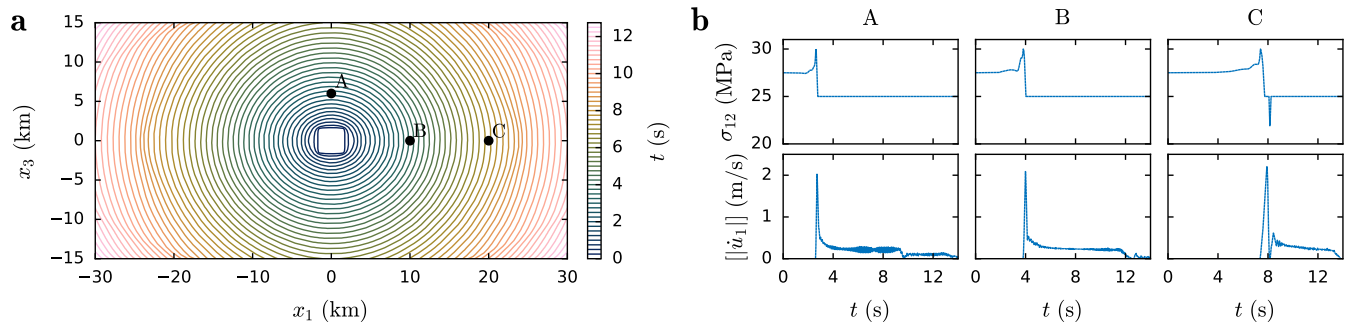


FIGURE 7 LVFZ setup solved using hybrid method with $\Delta x = 100$ m. (a) Contour of rupture front position each 0.5s. (b) Fault shear stress, σ_{12} , and slip rate, $||\dot{u}_1||$ at three stations A, B, and C with position shown in (a). At station C the rupture has split into a slip-pulse followed by a crack-like rupture.

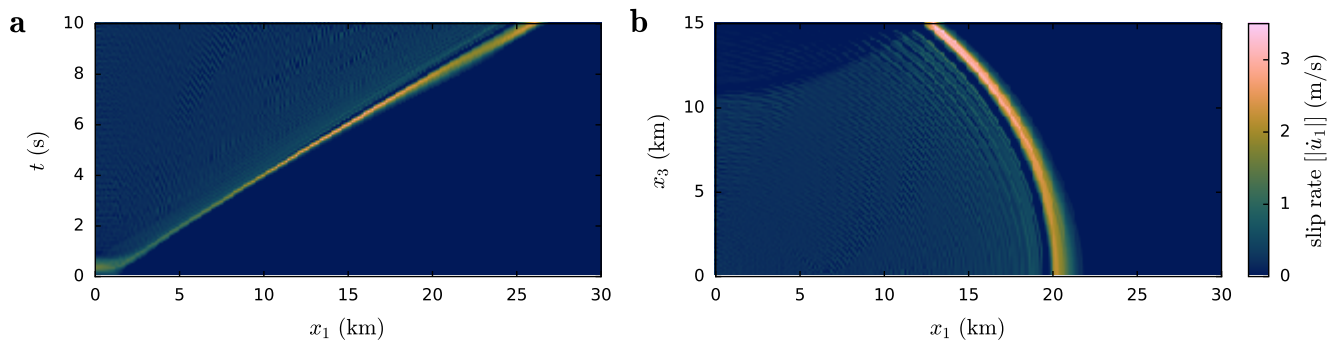


FIGURE 8 Pulse like rupture induced by LVFZ. (a) Space-time diagram of slip rate $[|\dot{u}_1|]$ along the symmetry axis $x_3 = 0$ km. At $t \approx 5$ s, the rupture splits into a slip-pulse, followed by a crack-like rupture. (b) Slip rate $[|\dot{u}_1|]$ at $t = 8$ s shows the spatial extent of the pulse-like and crack-like rupture.

238 5 | EARTHQUAKE RUPTURE IN A HETEROGENEOUS MEDIUM: SUPERSHEAR 239 TRANSITION

240 5.1 | Setup

241 The second showcase example, presented in this section, is similar to the previous example but with the more compliant material
242 being the one at a distance from the fault. We consider a slip-weakening fault with an off-fault low velocity zone. This case
243 could occur when a fault ruptures and interacts with the LVFZ of a nearby mature fault.^{50,54} We use the same geometry, friction
244 and elastic properties, and nucleation procedure as in Section 4 but consider the fault to be embedded in the reference material,
245 while beyond a distance $L^{FZ}/2$ from the fault plane the material has a 20% velocity reduction.

246 5.2 | Results

247 Similar as in the LVFZ setup of Sec. 4, elastic waves are reflected at the boundary of the low velocity inclusion and affect the
248 shear stress at the interface. However, the reflected waves have the same polarity as the incident ones and, hence, increase the
249 shear stress in front of the propagating rupture front (see Fig. 9b). This increasing shear stress peak eventually causes the rupture
250 to transition from subRayleigh to supershear velocities (see Fig. 9a and Fig. 10). SubRayleigh propagation occurs when the
251 rupture speed is lower than the Rayleigh wave speed, $c_R \approx 0.9c_s$, and can be observed at stations A and B in Fig. 9. Supershear
252 propagation, however, refers to ruptures propagating faster than c_s and their speed can approach the limiting speed, c_p .^{56,57} In
253 our simulations, supershear rupture occurs within the domain surrounding station C in Fig. 9a.

254 In this 3D simulation, we observe a supershear transition through the Burridge-Andrews mechanism,^{58,6} where a shear stress
255 peak in front of the existing crack nucleates the supershear rupture (see Fig. 9b, station B and Fig. 10). In contrast to 2D
256 setups,^{50,54} the extent of the supershear rupture is confined to a triangular shaped region, which surrounds station C. Additionally,
257 the transition occurs progressively: first at $x_3 = 0$ km at $t \approx 7$ s, then it expands towards the $\pm e_3$ direction, and finally, at $t \approx 12$ s
258 it spans the entire seismogenic depth.

259 This example illustrates the ability of the hybrid method of successfully truncating the shear Mach front, radiated from the
260 supershear rupture, without artificial reflections. Which allows us place the virtual boundary S^\pm at only $2\Delta x$ from the the
261 boundary of the low velocity inclusion. As in the previous problem, we validate the results of the hybrid method by varying the
262 width of the virtual strip, L_2 . The solution is found to be independent on L_2 .

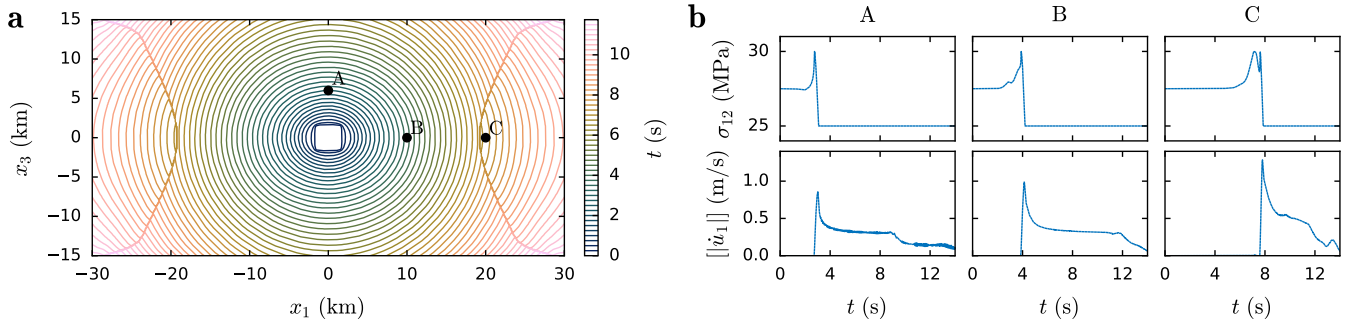


FIGURE 9 Off-fault low velocity zone setup solved using hybrid method with $\Delta x = 100$ m. (a) Contour of rupture front position each 0.5s. Widely spaced contour lines represent supershear propagation region. (b) Fault shear stress, σ_{12} , and slip rate, $||\dot{u}_1||$ at three stations A, B, and C with position shown in (a).

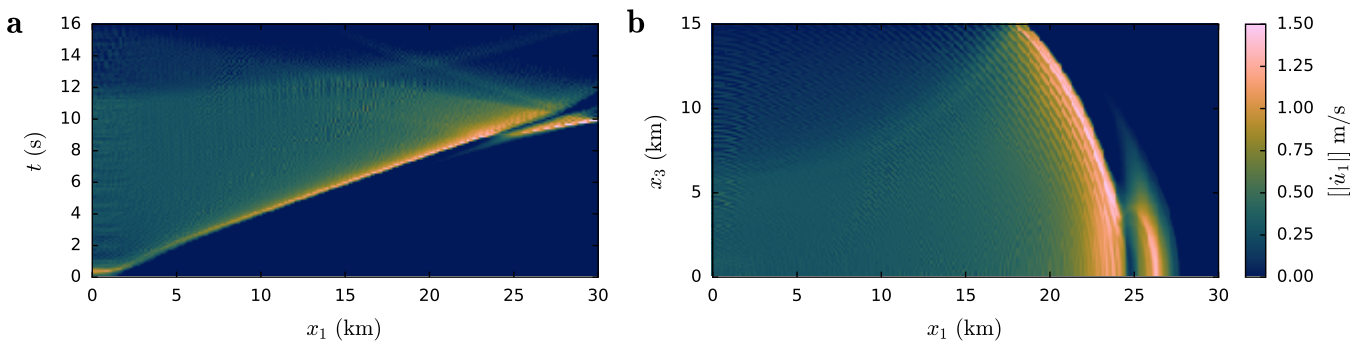


FIGURE 10 Supershear transition induced by off-fault low velocity zone. (a) Space-time diagram of slip rate $||\dot{u}_1||$ along the symmetry axis $x_3 = 0$ km. The rupture transitions to supershear at $x_1 \approx 24$ km. (b) Slip rate at $t = 9.25$ s shows the spatial extent of the supershear rupture, just after the transition has initiated.

6 | EARTHQUAKE RUPTURE WITH STEP-OVER FAULTS

6.1 | Setup

Finally, we present an example of interaction between nearby faults, *i.e.* two fracture planes side-by-side. We consider a dilational step-over geometry with a system of two faults that overlap each other (see Fig. 11). The dilational step-over implies that the location of the secondary fault with respect to the primary one is such that the rupture propagation on the primary fault will cause a temporary reduction in normal stress. The faults have uniform friction properties, $\mu_s = 0.677$, $\mu_k = 0.373$ and $d_c = 0.5$ m, except on the top 1 km of the seismogenic zone, where a slip-strengthening condition is imposed. At the bottom, *i.e.*, $x_3 < L_3^{rpt}$, we consider a no slip boundary condition and the nucleation is achieved by an instantaneous reduction of the friction strength over a region of size $a \times L_3^{rpt}$ to its kinetic value. This setup is analogous to a recent study by Bai and Ampuero.⁵⁹ The elastic properties are the same as in Section 3. We choose a seismogenic depth, $L_3^{rpt} = 10$ km and uniform background shear $\tau_0 = 71.2$ MPa and normal stress $\sigma_0 = 150$ MPa. Hence, the strength ratio is $S = (\mu_s \sigma_0 - \tau_0) / (\tau_0 - \mu_k \sigma_0) = 1.75$, and the condition for the rupture to jump from one fault to the adjacent one is satisfied.⁵⁹

Note that in this example there are no symmetries. In contrast to the previous examples where the fault plane represented a symmetry axis. As a result of the slip propagation on the primary fault, the normal stress on the secondary fault is not constant. The change in normal stress can reduce or increase the friction strength on the secondary fault, depending on their relative position. Thus, it can hinder or promote the rupture to jump between faults.

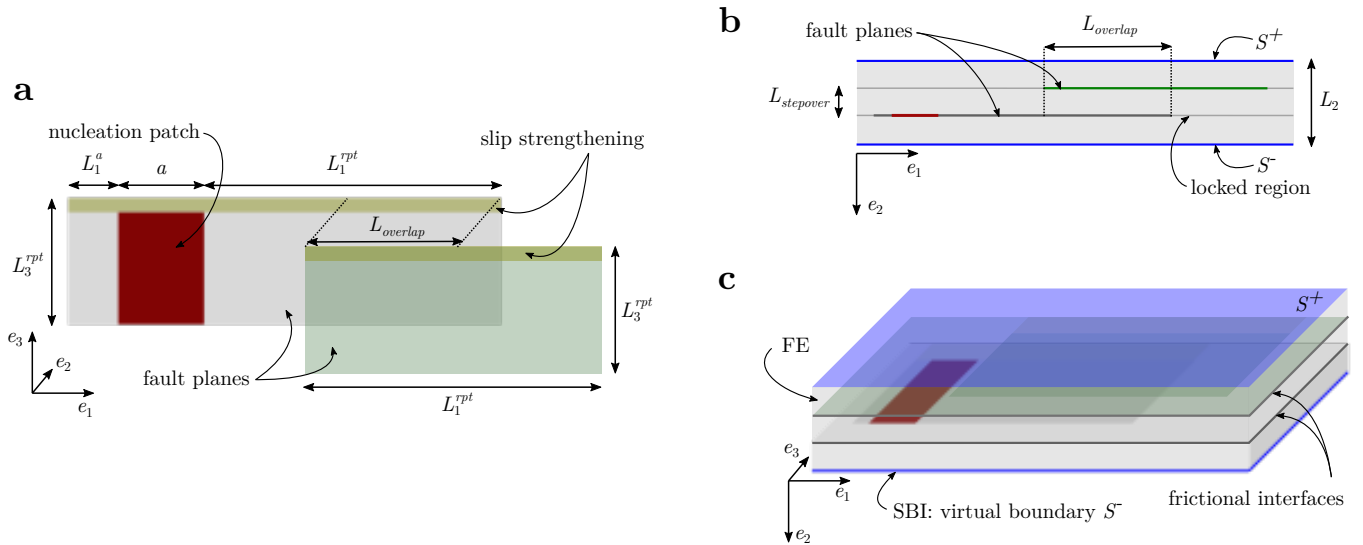


FIGURE 11 Setup of example earthquake rupture in unbounded domain with interacting parallel faults with step-over geometry. (a) Setup geometry. Fault zone regions of rectangular size with $L_1^{rpt} = 40$ km and $L_3^{rpt} = 10$ km, with nucleation over a width $a = 20$ km and the entire seismogenic depth, L_3^{rpt} . To the left of the nucleation patch the extent of the primary fault is $L_1^a = 10$ km. The two fault step-over geometry is characterized by $L_{overlap} = 20$ km and $L_{stepover} = 1$ km, shown in (b). The faults are embedded in a homogeneous elastic medium. (b and c) Hybrid setup: FE domain with SBI as elastodynamic boundary condition. The virtual strip width is $L_2 = 1.4$ km.

279 6.2 | Results

280 Using the hybrid method, we can successfully reproduce the results of Bai and Ampuero⁵⁹ (see Fig. 12): after nucleation, the
 281 rupture propagates over the primary fault with a nearly vertical front, then the rupture jumps to the secondary fault and, as a
 282 consequence of the no-slip boundary condition beyond the depth L_3^{rpt} , the rupture becomes a slip pulse. The wave emitted by the
 283 primary rupture successfully nucleates a large rupture on the secondary fault in the forward direction. This example illustrates
 284 the ability of the hybrid method to efficiently solve a large and complex simulation and efficiently truncate all incident waves
 285 without any artificial reflections. To validate the results of the hybrid method we vary the width of the virtual strip, L_2 , and find
 286 that also for this example L_2 does not affect the solution.

287 7 | DISCUSSION

288 We used a SCEC benchmark problem to validate the hybrid method and then demonstrated its flexibility and superior perfor-
 289 mance on more complex and heterogeneous problems. The proposed hybrid method takes its flexibility to deal with nonlinearities
 290 or bulk heterogeneities from the FEM and its computational efficiency from the SBIM. In particular, since the SBIM provides a
 291 perfect wave absorption algorithm there is no artificial wave reflection at the virtual boundary. Thus, one can reduce the width
 292 of the FEM domain arbitrarily close to the nonlinear or heterogeneous region, as long as the constitutive relation of the bulk
 293 beyond the virtual strip can be assumed to be linear.

294 The computational savings of using the hybrid method – instead of a traditional FEM – can be assessed by considering the
 295 complexity of both FEM and SBIM. The complexity of an explicit FEM time step is proportional to the number of degrees
 296 of freedom of the FEM problem, *i.e.*, $\mathcal{O}(N_1 N_2 N_3)$, where N_i is the number of elements in the i -direction and we assume a
 297 regular mesh of hexagonal elements. Similarly, the complexity of an SBIM time step scales with its number of degrees of
 298 freedom $\mathcal{O}(N_1 N_3)$. We measured the computation time for a range of simulations with different discretizations and domain
 299 sizes, which confirms the linear relationship between computational cost and the number of degrees of freedom (see Fig. 13).
 300 The computational saving of the hybrid method compared to a standard FEM lies in the reduction of N_2 due to the truncation of
 301 the FE domain. Moreover, the added overhead cost of the SBI as wave absorption algorithm is in the same order of magnitude
 302 of only one layer of FE elements (see Fig. 13b). Therefore, it is practically negligible.

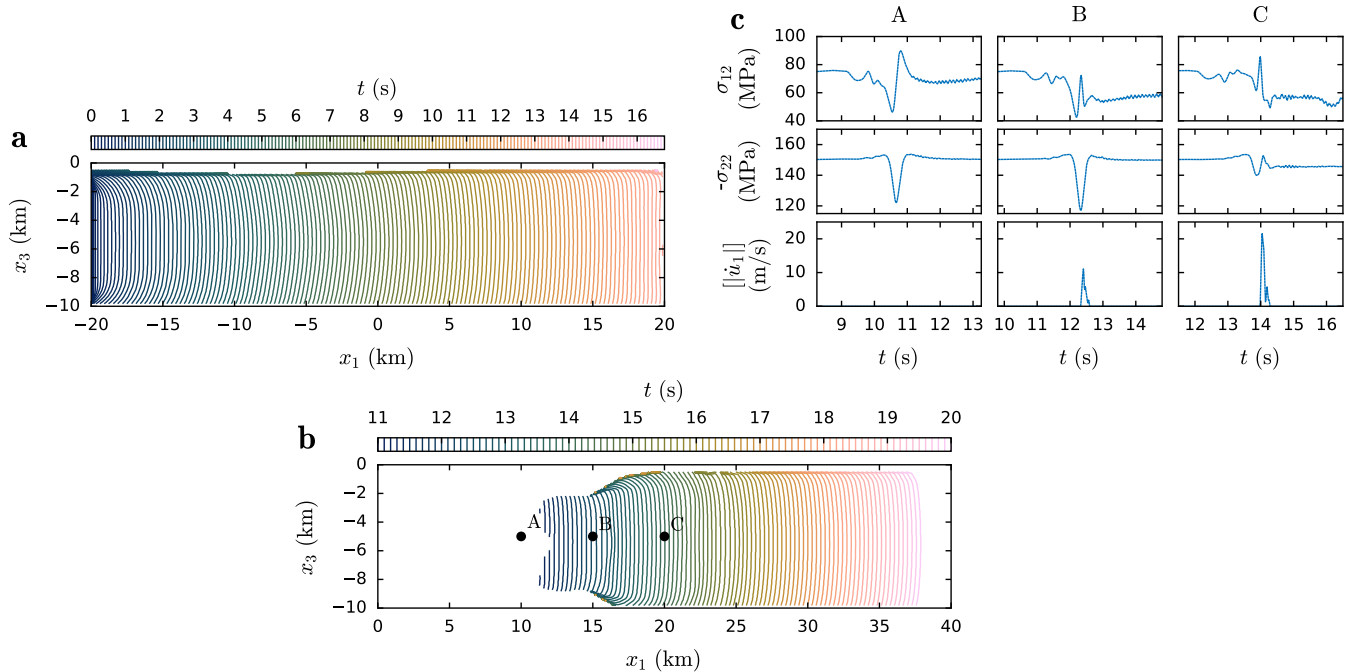


FIGURE 12 Results of example earthquake rupture in unbounded domain with interacting parallel faults with dilational step-over setup and spatial discretization $\Delta x = 100$ m. (a) Rupture front contour lines on primary fault, where nucleation occurs over region $-40 \text{ km} < x_1 < -20 \text{ km}$ (not shown). (b) Rupture front contour lines on secondary fault. Rupture transitions from primary to secondary fault. (c) Fault shear, σ_{12} , and normal, σ_{22} , stress and slip rate, $|\dot{u}_1|$ at three stations A, B, and C with position on the secondary fault shown in (b).

303 For example, for a full FE simulation, L_2 must be in the order of L_1 to prevent artificial reflections at the domain boundary.
 304 However, using the hybrid method the domain size can be truncated up to the extent of the nonlinear region or the extent
 305 of the elastic heterogeneity, which are usually one to two orders of magnitude smaller than L_1 .⁵⁰ Assuming a regular spatial
 306 discretization, the domain truncation results in a reduction of N_2 by one order of magnitude and so will the computational cost.
 307 The savings may be even higher in other applications.

308 All our simulations were performed using distributed memory parallel computing with 48 threads and for the largest simu-
 309 lations 96 threads. Therefore, in Fig. 13, we report the computational time multiplied by the number of parallel processes.
 310 However, the SBIM library that we are using also supports shared memory parallelism and it is designed to be easily coupled
 311 to any FEM library written in C++. The only requirement is that the FEM mesh at the virtual boundary S^\pm is a regular grid,
 312 due to the spectral representation of the boundary integral equations.

313 These computational savings represent an important step towards feasible modelling of complex temporal and spatial multi-
 314 scale 3D problems such as earthquake cycle simulations with near field heterogeneities, nonlinear material behavior and
 315 plasticity, as well as a networks of interacting faults, including fault branches and non-planar fault geometry. The major chal-
 316 lenge of earthquake cycle simulations is that they involve very long interseismic loading time (years) while the dynamic rupture
 317 happens extremely rapidly (seconds). An advantage of the hybrid method is that the SBIM is already capable of absorbing elas-
 318 tic waves in the dynamic as well as in the quasi-dynamic limit and these approaches can be combined in a variable time stepping
 319 scheme, introduced by Lapusta et al.² Such a temporal multi-scale simulation couples a quasi-dynamic SBIM with an implicit
 320 FEM during the slow loading phase and, once the ruptures become dynamic, it switches to a dynamic SBIM coupled with an
 321 explicit FEM – as considered in the current study. These variable time-stepping hybrid method was introduced in a 2D antiplane
 322 framework³¹ and will be extended to 3D in future work.

323 Another advantage of the hybrid method is that it could be implemented with any volume based method. For example, if the
 324 fault plane is not known a priori, one could use discretization techniques with embedded discontinuities, such as the XFEM⁶⁰
 325 or the discontinuous Galerkin.¹⁹

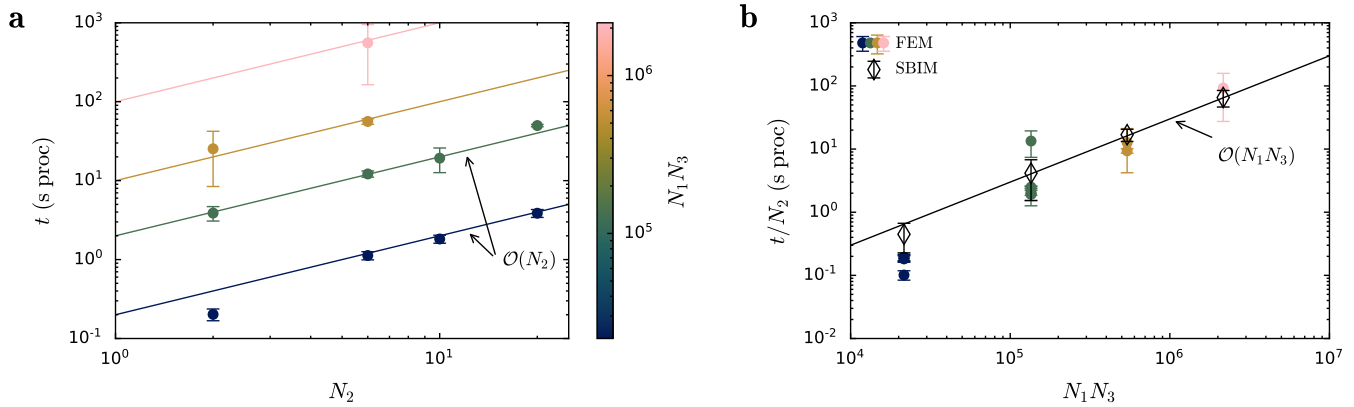


FIGURE 13 Performance study of FEM and Hybrid method. (a) Computation time, t , of a FEM time step as function of width of the virtual strip, *i.e.*, number of elements, N_2 . Scaling of computational time is shown for a range of frictional interface discretizations, $N_1 N_3$. The complexity of the FEM time step is linear in N_2 . (b) Computation time of the FEM time step, t , normalized by N_2 (same data and color-code as in (a)). The computation time of a SBIM time step, when computing the elastodynamic boundary condition for the virtual strip, is equivalent to the computation time for one layer of FEM elements. Both, FEM and SBIM computation times are linear in $N_1 N_3$.

8 | CONCLUSION

We developed a three dimensional hybrid method combining the finite-element method with the spectral boundary-integral method. We validated the hybrid method using a benchmark problem and illustrated its potential for solving complex earthquake propagation on various example problems including near systems with field heterogeneity and multiple interacting faults. The hybrid method is suitable for cases where the spatial extent of near field nonlinearity and heterogeneity is too large to be lumped into an effective fault constitutive law, but is still considerably smaller than the domain of interest for the wave propagation. In these cases, the hybrid method allows for a reduction of computational cost by at least one order of magnitude with respect to a full finite-element implementation, while maintaining the same level of accuracy. The high accuracy and computational efficiency of the hybrid method enable the investigation of complex failure problems such as multi-physics fault zone problems.

ACKNOWLEDGMENTS

The authors thank Dr. Nicolas Richart for technical help.

References

1. Noda H, Dunham EM, Rice JR. Earthquake ruptures with thermal weakening and the operation of major faults at low overall stress levels. *Journal of Geophysical Research: Solid Earth* 2009; 114(B7). [_eprint: https://onlinelibrary.wiley.com/doi/pdf/10.1029/2008JB006143](https://onlinelibrary.wiley.com/doi/pdf/10.1029/2008JB006143)doi: <https://doi.org/10.1029/2008JB006143>
2. Lapusta N, Rice JR, Ben-Zion Y, Zheng G. Elastodynamic analysis for slow tectonic loading with spontaneous rupture episodes on faults with rate- and state-dependent friction. *Journal of Geophysical Research: Solid Earth* 2000; 105(B10): 23765–23789. doi: 10.1029/2000JB900250
3. Cochard A, Madariaga R. Dynamic faulting under rate-dependent friction. *pure and applied geophysics* 1994; 142(3): 419–445. doi: 10.1007/BF00876049
4. Geubelle PH, Rice JR. A spectral method for three-dimensional elastodynamic fracture problems. *Journal of the Mechanics and Physics of Solids* 1995; 43(11): 1791–1824. doi: 10.1016/0022-5096(95)00043-I

- 348 5. Boore DM, Aki K, Todd T. A two-dimensional moving dislocation model for a strike-slip fault. *Bulletin of the Seismological*
349 *Society of America* 1971; 61(1): 177–194.
- 350 6. Andrews DJ. Rupture velocity of plane strain shear cracks. *Journal of Geophysical Research* 1976; 81(32): 5679–5687. doi:
351 10.1029/JB081i032p05679
- 352 7. Das S, Aki K. A numerical study of two-dimensional spontaneous rupture propagation. *Geophysical Journal of the Royal*
353 *Astronomical Society* 1977; 50(3): 643–668. doi: 10.1111/j.1365-246X.1977.tb01339.x
- 354 8. Archuleta RJ, Day SM. Dynamic rupture in a layered medium: The 1966 Parkfield earthquake. *Bulletin of the Seismological*
355 *Society of America* 1980; 70(3): 671–689.
- 356 9. Day SM. Three-dimensional simulation of spontaneous rupture: The effect of nonuniform prestress. *Bulletin of the*
357 *Seismological Society of America* 1982; 72(6A): 1881–1902.
- 358 10. Virieux J, Madariaga R. Dynamic faulting studied by a finite difference method. *Bulletin of the Seismological Society of*
359 *America* 1982; 72(2): 345–369.
- 360 11. Komatitsch D, Tromp J. Introduction to the spectral element method for three-dimensional seismic wave propagation.
361 *Geophysical Journal International* 1999; 139(3): 806–822. doi: 10.1046/j.1365-246x.1999.00967.x
- 362 12. AMPUERO JP. Etude physique et numerique de la nucleation des seismes. *PhD Thesis, University of Paris VII, France*
363 2002.
- 364 13. Festa G, Vilotte JP. Influence of the rupture initiation on the intersonic transition: Crack-like versus pulse-like modes.
365 *Geophysical Research Letters* 2006; 33(15). _eprint: <https://onlinelibrary.wiley.com/doi/pdf/10.1029/2006GL026378>doi:
366 <https://doi.org/10.1029/2006GL026378>
- 367 14. Ma S, Archuleta RJ. Radiated seismic energy based on dynamic rupture models of faulting. *Journal of Geophysi-*
368 *cal Research: Solid Earth* 2006; 111(B5). _eprint: <https://onlinelibrary.wiley.com/doi/pdf/10.1029/2005JB004055>doi:
369 <https://doi.org/10.1029/2005JB004055>
- 370 15. Kaneko Y, Lapusta N, Ampuero JP. Spectral element modeling of spontaneous earthquake rupture on rate and state faults:
371 Effect of velocity-strengthening friction at shallow depths. *Journal of Geophysical Research: Solid Earth* 2008; 113(B9).
372 _eprint: <https://onlinelibrary.wiley.com/doi/pdf/10.1029/2007JB005553>doi: 10.1029/2007JB005553
- 373 16. Käser M, Dumbser M. An arbitrary high-order discontinuous Galerkin method for elastic waves on unstructured meshes
374 — I. The two-dimensional isotropic case with external source terms. *Geophysical Journal International* 2006; 166(2):
375 855–877. doi: 10.1111/j.1365-246X.2006.03051.x
- 376 17. Benjema M, Glinsky-Olivier N, Cruz-Atienza VM, Virieux J, Piperno S. Dynamic non-planar crack rupture by a finite
377 volume method. *Geophysical Journal International* 2007; 171(1): 271–285. doi: 10.1111/j.1365-246X.2006.03500.x
- 378 18. Puente Jdl, Ampuero JP, Käser M. Dynamic rupture modeling on unstructured meshes using a dis-
379 continuous Galerkin method. *Journal of Geophysical Research: Solid Earth* 2009; 114(B10). _eprint:
380 <https://onlinelibrary.wiley.com/doi/pdf/10.1029/2008JB006271>doi: <https://doi.org/10.1029/2008JB006271>
- 381 19. Pelties C, Puente Jdl, Ampuero JP, Brietzke GB, Käser M. Three-dimensional dynamic rupture simulation
382 with a high-order discontinuous Galerkin method on unstructured tetrahedral meshes. *Journal of Geophysical*
383 *Research: Solid Earth* 2012; 117(B2). _eprint: <https://onlinelibrary.wiley.com/doi/pdf/10.1029/2011JB008857>doi:
384 <https://doi.org/10.1029/2011JB008857>
- 385 20. Tago J, Cruz-Atienza VM, Virieux J, Etienne V, Sánchez-Sesma FJ. A 3D hp-adaptive discontinuous Galerkin
386 method for modeling earthquake dynamics. *Journal of Geophysical Research: Solid Earth* 2012; 117(B9). _eprint:
387 <https://onlinelibrary.wiley.com/doi/pdf/10.1029/2012JB009313>doi: <https://doi.org/10.1029/2012JB009313>
- 388 21. Cruz-Atienza VM, Virieux J, Aochi H. 3D finite-difference dynamic-rupture modeling along nonplanar faults. *GEO-*
389 *PHYSICS* 2007; 72(5): SM123–SM137. Publisher: Society of Exploration Geophysicistsdoi: 10.1190/1.2766756

- 390 22. Dalguer LA, Day SM. Staggered-grid split-node method for spontaneous rupture simulation. *Journal of Geophysical Research: Solid Earth* 2007; 112(B2). _eprint: <https://onlinelibrary.wiley.com/doi/pdf/10.1029/2006JB004467>
391 <https://doi.org/10.1029/2006JB004467>
392
- 393 23. Kozdon JE, Dunham EM, Nordström J. Simulation of Dynamic Earthquake Ruptures in Complex Geometries Using High-
394 Order Finite Difference Methods. *Journal of Scientific Computing* 2013; 55(1): 92–124. doi: 10.1007/s10915-012-9624-5
- 395 24. Lysmer J, Kuhlemeyer RL. Finite Dynamic Model For Infinite Media. *Journal of the Engineering Mechanics Division* 1969;
396 95(4): 859–878. Publisher: ASCE.
- 397 25. Berenger JP, others . A perfectly matched layer for the absorption of electromagnetic waves. *Journal of computational*
398 *physics* 1994; 114(2): 185–200. Publisher: New York, Academic Press.
- 399 26. Bettess P. Infinite elements. *International Journal for Numerical Methods in Engineering* 1977; 11(1): 53–64. _eprint:
400 <https://onlinelibrary.wiley.com/doi/pdf/10.1002/nme.1620110107>doi: <https://doi.org/10.1002/nme.1620110107>
- 401 27. Erickson BA, Day SM. Bimaterial effects in an earthquake cycle model using rate-and-state
402 friction. *Journal of Geophysical Research: Solid Earth* 2016; 121(4): 2480–2506. _eprint:
403 <https://onlinelibrary.wiley.com/doi/pdf/10.1002/2015JB012470>doi: <https://doi.org/10.1002/2015JB012470>
- 404 28. Hajarolasvadi S, Elbanna AE. A new hybrid numerical scheme for modelling elastodynamics in unbounded media with
405 near-source heterogeneities. *Geophysical Journal International* 2017; 211(2): 851–864. doi: 10.1093/gji/ggx337
- 406 29. Ma X, Hajarolasvadi S, Albertini G, Kammer DS, Elbanna AE. A hybrid finite element-spectral boundary integral approach:
407 Applications to dynamic rupture modeling in unbounded domains. *International Journal for Numerical and Analytical*
408 *Methods in Geomechanics* 2019; 43(1): 317–338. doi: 10.1002/nag.2865
- 409 30. Ma X, Elbanna A. Dynamic rupture propagation on fault planes with explicit representation of short branches. *Earth and*
410 *Planetary Science Letters* 2019; 523: 115702. doi: 10.1016/j.epsl.2019.07.005
- 411 31. Abdelmeguid M, Ma X, Elbanna A. A Novel Hybrid Finite Element-Spectral Boundary Integral Scheme for Modeling
412 Earthquake Cycles: Application to Rate and State Faults With Low-Velocity Zones. *Journal of Geophysical Research:*
413 *Solid Earth* 2019; 124(12): 12854–12881. _eprint: <https://onlinelibrary.wiley.com/doi/pdf/10.1029/2019JB018036>doi:
414 <https://doi.org/10.1029/2019JB018036>
- 415 32. Day SM, Dalguer LA, Lapusta N, Liu Y. Comparison of finite difference and boundary integral solutions to three-
416 dimensional spontaneous rupture. *Journal of Geophysical Research: Solid Earth* 2005; 110(B12): B12307. doi:
417 10.1029/2005JB003813
- 418 33. Ida Y. Cohesive force across the tip of a longitudinal-shear crack and Griffith's specific surface energy. *Journal of*
419 *Geophysical Research* 1972; 77(20): 3796–3805. doi: 10.1029/JB077i020p03796
- 420 34. Dieterich JH. Modeling of rock friction: 2. Simulation of preseismic slip. *Journal of Geophysical Research:*
421 *Solid Earth* 1979; 84(B5): 2169–2175. _eprint: <https://onlinelibrary.wiley.com/doi/pdf/10.1029/JB084iB05p02169>doi:
422 10.1029/JB084iB05p02169
- 423 35. Ruina A. Slip instability and state variable friction laws. *Journal of Geophysical Research: Solid Earth* 1983; 88(B12):
424 10359–10370. doi: 10.1029/JB088iB12p10359
- 425 36. Belytschko T, Liu WK, Moran B, Elkhodary K. *Nonlinear Finite Elements for Continua and Structures*. Wiley . 2013.
- 426 37. Courant R, Friedrichs K, Lewy H. Über die partiellen Differenzgleichungen der mathematischen Physik. *Mathematische*
427 *Annalen* 1928; 100(1): 32–74. doi: 10.1007/BF01448839
- 428 38. Carpenter NJ, Taylor RL, Katona MG. Lagrange constraints for transient finite element surface con-
429 tact. *International Journal for Numerical Methods in Engineering* 1991; 32(1): 103–128. _eprint:
430 <https://onlinelibrary.wiley.com/doi/pdf/10.1002/nme.1620320107>doi: <https://doi.org/10.1002/nme.1620320107>

- 431 39. Das S. A numerical method for determination of source time functions for general three-dimensional rupture propagation.
432 *Geophysical Journal International* 1980; 62(3): 591–604. doi: 10.1111/j.1365-246X.1980.tb02593.x
- 433 40. Andrews DJ. Dynamic plane-strain shear rupture with a slip-weakening friction law calculated by a boundary integral
434 method. *Bulletin of the Seismological Society of America* 1985; 75(1): 1–21.
- 435 41. Boatwright J, Quin H. The Seismic Radiation from a 3-D Dynamic Model of a Complex Rupture Pro-
436 cess. Part I: Confined Ruptures. In: American Geophysical Union (AGU). 1986 (pp. 97–109). _eprint:
437 <https://onlinelibrary.wiley.com/doi/pdf/10.1029/GM037p0097>
- 438 42. Das S, Kostrov BV. On the Numerical Boundary Integral Equation Method for Three-Dimensional Dynamic Shear Crack
439 Problems. *Journal of Applied Mechanics* 1987; 54(1): 99–104. doi: 10.1115/1.3173002
- 440 43. Das S, Kostrov BV. An investigation of the complexity of the earthquake source time function using
441 dynamic faulting models. *Journal of Geophysical Research: Solid Earth* 1988; 93(B7): 8035–8050. _eprint:
442 <https://onlinelibrary.wiley.com/doi/pdf/10.1029/JB093iB07p08035>doi: <https://doi.org/10.1029/JB093iB07p08035>
- 443 44. Israil A, Banerjee P. Two-dimensional transient wave-propagation problems by time-domain BEM. *International Journal*
444 *of Solids and Structures* 1990; 26(8): 851–864. doi: 10.1016/0020-7683(90)90073-5
- 445 45. Koller MG, Bonnet M, Madariaga R. Modelling of dynamical crack propagation using time-domain boundary integral
446 equations. *Wave Motion* 1992; 16(4): 339–366. doi: 10.1016/0165-2125(92)90022-T
- 447 46. Liu Y, Rizzo F. Hypersingular boundary integral equations for radiation and scattering of elastic waves in three dimensions.
448 *Computer Methods in Applied Mechanics and Engineering* 1993; 107(1-2): 131–144. doi: 10.1016/0045-7825(93)90171-S
- 449 47. Bonnet M, Bui HD. Regularization of the Displacement and Traction BIE for 3D Elastodynamics Using Indirect Meth-
450 ods. In: Kane JH, Maier G, Tosaka N, Atluri SN., eds. *Advances in Boundary Element Techniques* Springer Series in
451 Computational Mechanics. Berlin, Heidelberg: Springer. 1993 (pp. 1–29)
- 452 48. Andrews DJ. Dynamic growth of mixed-mode shear cracks. *Bulletin of the Seismological Society of America* 1994; 84(4):
453 1184–1198.
- 454 49. Breitenfeld MS, Geubelle PH. Numerical analysis of dynamic debonding under 2D in-plane and 3D loading. *International*
455 *Journal of Fracture* 1998; 93(1-4): 13–38. doi: 10.1023/A:1007535703095
- 456 50. Ma X, Elbanna A. Effect of off-fault low-velocity elastic inclusions on supershear rupture dynamics. *Geophysical Journal*
457 *International* 2015; 203(1): 664–677. doi: 10.1093/gji/ggv302
- 458 51. Huang Y, Ampuero JP. Pulse-like ruptures induced by low-velocity fault zones. *Journal of Geophysical Research* 2011;
459 116(B12). doi: 10.1029/2011JB008684
- 460 52. Huang Y, Ampuero JP, Helmberger DV. Earthquake ruptures modulated by waves in damaged fault zones. *Journal of*
461 *Geophysical Research: Solid Earth* 2014; 119(4): 2013JB010724. doi: 10.1002/2013JB010724
- 462 53. Huang Y, Ampuero JP, Helmberger DV. The potential for supershear earthquakes in damaged fault zones – theory and
463 observations. *Earth and Planetary Science Letters* 2016; 433: 109–115. doi: 10.1016/j.epsl.2015.10.046
- 464 54. Albertini G, Kammer DS. Off-fault heterogeneities promote supershear transition of dynamic mode II cracks. *Journal of*
465 *Geophysical Research: Solid Earth* 2017; 122(8): 2017JB014301. doi: 10.1002/2017JB014301
- 466 55. Kammer DS, Yastrebov VA, Anciaux G, Molinari JF. The existence of a critical length scale in regularised friction. *Journal*
467 *of the Mechanics and Physics of Solids* 2014; 63: 40–50. doi: 10.1016/j.jmps.2013.10.007
- 468 56. Freund LB. The mechanics of dynamic shear crack propagation. *Journal of Geophysical Research: Solid Earth* 1979;
469 84(B5): 2199–2209. doi: 10.1029/JB084iB05p02199

- 470 57. Kammer DS, Svetlizky I, Cohen G, Fineberg J. The equation of motion for supershear frictional rupture fronts. *Science*
471 *Advances* 2018; 4(7): eaat5622. Publisher: American Association for the Advancement of Science Section: Research
472 Articledoi: 10.1126/sciadv.aat5622
- 473 58. Burridge R. Admissible speeds for plane-strain self-similar shear cracks with friction but lacking cohesion. *Geophysical*
474 *Journal International* 1973; 35(4): 439–455.
- 475 59. Bai K, Ampuero JP. Effect of Seismogenic Depth and Background Stress on Physical Limits of Earthquake Rupture Across
476 Fault Step Overs: FAULT CRITICAL STEP OVER JUMP DISTANCE. *Journal of Geophysical Research: Solid Earth*
477 2017; 122(12): 10,280–10,298. doi: 10.1002/2017JB014848
- 478 60. Liu F, Borja RI. An extended finite element framework for slow-rate frictional faulting with bulk plasticity and variable
479 friction. *International Journal for Numerical and Analytical Methods in Geomechanics* 2009; 33(13): 1535–1560. _eprint:
480 <https://onlinelibrary.wiley.com/doi/pdf/10.1002/nag.777>doi: <https://doi.org/10.1002/nag.777>